remote sensing

MDPI

Technical Note

Towards a General Monitoring System for Terrestrial Primary Production: A Test Spanning the European Drought of 2018

Keith J. Bloomfield [1,*], Roel van Hoolst [2], Manuela Balzarolo [3], Ivan A. Janssens [3], Sara Vicca [3], Darren Ghent [4] and I. Colin Prentice [1,5]

[1] Georgina Mace Centre for the Living Planet, Department of Life Sciences, Imperial College London, Silwood Park Campus, Buckhurst Road, Ascot SL5 7PY, UK
[2] Flemish Institute for Technological Research (VITO), 2400 Mol, Belgium
[3] Department of Biology, University of Antwerp, 2610 Wilrijk, Belgium
[4] National Centre for Earth Observation (NCE), Department of Physics and Astronomy, University of Leicester, University Road, Leicester LE1 7RH, UK
[5] Ministry of Education Key Laboratory for Earth System Modelling, Department of Earth System Science, Tsinghua University, Beijing 100084, China
* Correspondence: k.bloomfield@imperial.ac.uk

Abstract: (1) Land surface models require inputs of temperature and moisture variables to generate predictions of gross primary production (GPP). Differences between leaf and air temperature vary temporally and spatially and may be especially pronounced under conditions of low soil moisture availability. The Sentinel-3 satellite mission offers estimates of the land surface temperature (LST), which for vegetated pixels can be adopted as the canopy temperature. Could remotely sensed estimates of LST offer a parsimonious input to models by combining information on leaf temperature and hydration? (2) Using a light use efficiency model that requires only a handful of input variables, we generated GPP simulations for comparison with eddy-covariance inferred estimates available from flux sites within the Integrated Carbon Observation System. Remotely sensed LST and greenness data were input from Sentinel-3. Gridded air temperature data were obtained from the European Centre for Medium-Range Weather Forecasts. We chose the years 2018–2019 to exploit the natural experiment of a pronounced European drought. (3) Simulated GPP showed good agreement with flux-derived estimates. During dry conditions, simulations forced with LST performed better than those with air temperature for shrubland, grassland and savanna sites. (4) This study advances the prospect for a global GPP monitoring system that will rely primarily on remotely sensed inputs.

Keywords: land surface temperature; drought; remote sensing; GPP; ICOS; eddy covariance

Citation: Bloomfield, K.J.; van Hoolst, R.; Balzarolo, M.; Janssens, I.A.; Vicca, S.; Ghent, D.; Prentice, I.C. Towards a General Monitoring System for Terrestrial Primary Production: A Test Spanning the European Drought of 2018. *Remote Sens.* **2023**, *15*, 1693. https://doi.org/10.3390/rs15061693

Academic Editor: Ernesto López-Baeza

Received: 16 February 2023
Revised: 9 March 2023
Accepted: 18 March 2023
Published: 21 March 2023

1. Introduction

Terrestrial gross primary production (GPP) is the largest flux in the global carbon cycle [1]. Anthropogenic disturbances to natural cycles include CO_2 emission to the atmosphere, but terrestrial vegetation provides a sink for a part of the emitted CO_2—driven primarily by the fact that the CO_2 concentration is nonetheless rising [2]. Currently our best, in situ estimates of GPP are provided by the eddy-covariance method that measures high-frequency net carbon fluxes between the canopy and the atmosphere [3]. Those measurements of net ecosystem exchange (NEE) can be partitioned into GPP and ecosystem respiration allowing empirical evaluation of model simulations of GPP. There are now hundreds of flux-tower sites [4] and collectively they provide the foundation and benchmark for global terrestrial vegetation monitoring. The technique has its difficulties, however—including how best to partition NEE into the component fluxes [5], the need for a reasonably flat and homogenous footprint [6] and under-representation of certain biomes (notably tropical biomes). These problems, together with the desire to provide spatially continuous estimates, have encouraged the development of remote-sensing models where

global fields of key drivers are provided by satellite-derived products. The overall goal of such research is to develop a global GPP monitoring system, based on a reliable model, driven by remotely sensed data and evaluated against flux-tower data.

The instantaneous controls of leaf-level photosynthesis are described by the FvCB model of C_3 photosynthesis [7] in which instantaneous carbon assimilation is limited either by Rubisco activity (carboxylation) or by light (electron transport). Both rates are influenced by the leaf-internal partial pressure of CO_2 (C_i). Empirical equations are commonly used to determine C_i, which depends on stomatal behaviour. Current eco-physiological theory, and most biophysical land-surface schemes for climate modelling, make use of the FvCB model.

The instantaneous photosynthetic response to light, as observed experimentally and represented in the FvCB model, is a non-linear (saturating) function. A different relationship with light emerges, however, at longer timescales [8,9]. Based on measurements of crop growth, Monteith [10,11] proposed the light-use efficiency (LUE) model (GPP = LUE $\times$ IPAR $\times$ fAPAR) where IPAR is the incident photosynthetically active radiation and fAPAR the fraction absorbed by green vegetation. There are now many LUE models in the literature [12], but no consensus on which is best. There has also been a marked tendency for these models to become more complex and to require more parameters, but without necessarily increasing in accuracy [13].

The P model [14] is a LUE model based on optimality principles that coordinate capacities for CO_2 fixation, water- and electron-transport to simulate GPP consistent with the FvCB framework. The model can be applied universally to C_3 plants with no need for biome-specific parameters. The P model as deployed here is the 'BRC' version presented by Stocker et al. [15] with a modification [16] to describe C_4 photosynthesis. This version differs from the original model of Wang et al. principally by representing the temperature-dependence of the intrinsic quantum efficiency of photosynthesis, which was described by Bernacchi et al. [17], but is neglected in many current models [18]. Stocker et al. (2020) also introduced a single global calibration parameter to optimize agreement between P model simulations and flux data. In a departure from the approach of Stocker et al., we have here assigned the maximum quantum efficiency its theoretical upper bound of 0.125 (eight quanta per CO_2 reduced), eliminating the need for calibration.

GPP is expected to be influenced by temperature because of the various temperature-dependent quantities that affect photosynthetic rates [17,19]. The instantaneous temperature response of leaf-level photosynthesis is unimodal with photosynthesis inhibited at low and high temperatures, reaching an optimum somewhere in between [20]. But the optimum acclimates to growth conditions [21], and it is challenging to determine whether foliage is operating above or below the current optimum. There can also be differences between the temperature of the leaf and that of the ambient air [22]; those differences (or deltas) are influenced by radiation, transpiration and boundary-layer conductance [23,24]. It would be desirable to replace measures of air temperature with remotely sensed land surface temperature (LST): theoretically, because LST is expected to be closer to the actual temperature of leaf tissue relevant for physiological processes; and practically, because remotely sensed LST is retrieved at a high spatial resolution relative to weather-station or meteorological analysis data.

Stomata are the conduits both for CO_2 into the leaf, and for the loss of water vapour via transpiration. Stomata respond to an increase in vapour pressure deficit (VPD) by progressively closing to limit transpiration and this entrains a reduction in photosynthesis [25,26]. Drought events, such as those experienced in central Europe in 2018 [27], can have further profound effects on vegetation and its productivity by causing earlier stomatal closure in response to VPD. Ciais et al. [28] estimated that the 2003 heatwave instigated a 30% reduction in GPP across Europe, upsetting the continental carbon balance and, in the short-term, converting the region from a sink to a source of CO_2. This effect of drought can interact with elevated temperatures to create a positive feedback loop—soil water depletion reducing evaporative cooling. In common with many LUE models, the P model does not take account of soil moisture effects, except as manifested through changes in fAPAR.

Existing remotely sensed measures of soil moisture [29] are unable to give information about the moisture content of deeper soil layers that can be essential for plant function.

The incremental predictive power of soil moisture estimates for GPP, when VPD values are available, is open to question [30]. Indeed, in the field and on relatively moist soils, soil moisture content has little or no effect on LUE. Analysis of flux-based GPP measurements at the sites considered by Wang et al. [14], including a number of sites with pronounced dry seasons, confirmed that there is no universal decline of LUE with decreasing soil moisture, the implication being that any drought-induced reduction of GPP is already largely accounted for through the response of fAPAR. Changes in vegetation function, however, may not always be accompanied by changes in the state or extent of the foliage. A number of studies have reported the inability of remote sensing products to accurately capture drought effects on productivity. Vicca et al. [31] compared the performance of a suite of 11 satellite-based products (including fAPAR and prevalent greenness indices) in predicting GPP for a decadal timeseries (ca. 2000–2012) at four European sites (a mix of forests and grassland) and reported contrasting results—no single product proved capable of capturing each drought event at each site. Independent of leaf cover, some ecosystems (for example, tropical savannas and Mediterranean-type forests) regularly show reduced LUE during part or all of the dry season [32]. Moreover, extreme droughts to which ecosystems are not well adapted are expected to suppress LUE via a combination of reduced C_i and (under the most severe drying) reduced carboxylation capacity, as has been observed in drying-down experiments [33]. Therefore, in common with other operational products, the P model, when driven by air temperature, is likely to overestimate dry-season GPP in some ecosystems, and to underestimate the negative effect of extreme droughts on GPP [34]. When, however, air temperature is replaced with LST as a driver, the P model should implicitly take some account of the effect of drought-induced stomatal closure on transpiration and on GPP.

Exploiting the natural experiment provided by the European drought of 2018, this study aimed to evaluate the performance of the P model in simulating spatial and seasonal variability of GPP for a variety of ecosystems. We hypothesised that agreement with flux-derived GPP estimates would be stronger for simulations forced with LST versus gridded meteorological air temperature and superior performance would be most evident in dry summers.

2. Materials and Methods

2.1. Validation Data

The validation dataset was drawn from the Integrated Carbon Observation System (ICOS) measurement sites situated across Europe. ICOS eddy-covariance flux data are processed and audited consistent with the pipeline methodology developed within the FLUXNET network [4]. For this study, in order to match compatible satellite-derived data available only post 2016 (Sentinel3), we elected to focus on the years 2018 and 2019 employing the 'Warm Winter 2020' dataset, first release. A total of 69 sites were considered. Data exploration steps (e.g., screening for gaps of greater than two months) reduced the final dataset to 64 sites (Table A1, Figure A1, Appendix A). Vegetation categories follow the IGBP land cover classification: evergreen needleleaf forest (ENF), deciduous broadleaf forest (DBF), mixed forest (MF), closed shrublands (CSH), open shrublands (OSH), savannahs (SAV), grasslands (GRA), permanent wetlands (WET) and croplands (CRO).

Daily GPP data (gC m^{-2} d^{-1}) were based on the day-time flux decomposition method and the filtering based on a variable friction velocity threshold (GPP_DT_VUT_USTAR50). We retained only those days for which less than 20% of the underlying half-hourly meteorological and flux data were gap-filled. Our analysis is based on ten-day averages. This was the preferred timescale as voted in a user survey and mirrors the commonly adopted timestep for remote sensing products such as the Copernicus Land Monitoring Service.

2.2. Drought Index

In order to identify those periods when sites were experiencing drought conditions, we employed the Standardized Evapotranspiration–Precipitation Index (SPEI), a commonly used indicator of drought [35,36]. SPEI values were generated for each site using a three-decade time series (1989–2021 inclusive) of climatic water balance (precipitation minus potential evapotranspiration, European Centre for Medium-range Weather Forecasts (ECMWF)) via the *R* package 'SPEI' [37]. Unusually dry conditions, for a given site, were characterised as those time points with SPEI less than −1.5 [31].

2.3. Driving Variables for the P Model Simulations

GPP simulations were generated using the P-model and implemented via the *R* package 'rpmodel' [15,38]. Here, we used a formulation of the P-model that does not account for soil moisture stress, but with an updated formulation for the temperature sensitivity of quantum yield in C_4 plants (see below).

Solar radiation and vapour pressure data were obtained from the ECMWF high-resolution forecast model. These data (available in 0.25° grid cells) are operational forecasts for the next 24 h obtained via the MeteoGroup operational forecast system: (https://www.ecmwf.int/en/forecasts/datasets/set-i, accessed on 11 May 2021). IPAR data were derived from global radiation and converted to PPFD using the conversion factor 2.04 μmol J^{-1} [39]. The vapour pressure deficit was calculated from vapour pressure and air temperature following Allen et al. [40].

Daily temperature data were obtained from (a) gridded ECMWF meteorological data as described above (T_{air}, °C); and (b) from remotely sensed LST using daily level 3C Sentinel-3A SLSTR [41] obtained via the ESA project Land Surface Temperature Climate Change Initiative (https://climate.esa.int/en/projects/land-surface-temperature/about/, accessed on 7 July 2021). Pre-processing of these LST data involved cloud/confidence masking, separating day- and night-time overpasses, and interpolation using a cubic smoothing spline (function smooth.spline () with parameter spar = 0.01 in *R*) to provide ten-day averages based on the daytime overpass (typically mid-morning *ca* 10:00).

fAPAR data were obtained from the operational Sentinel-3 ESA Full Resolution OLCI product (OL_2_LFR, https://sentinel.esa.int/web/sentinel/user-guides/sentinel-3-olci/product-types/level-2-land, accessed on 12 May 2021). The OGVI (OLCI Global Vegetation Index) and "OGVI_err" band contain respectively the instantaneous green fAPAR and associated product uncertainties. Pre-processing implemented the associated LQSF layer (classification, quality, and science flags) to remove clouds and cloud shadows. The remaining data were further smoothed, and gap-filled, with a Gaussian process regression (https://scikit-learn.org/stable/modules/gaussian_process.html, accessed on 13 May 2021) algorithm, that allows the propagation of the initial data uncertainties to the gap-filled time series. The resulting output series were mapped to a 10-day interval.

Annual values of the CO_2 mole fraction were obtained from the monitoring station at Mauna Loa, Hawaii (Scripps Institution CO_2 monitoring network: http://scrippsco2.ucsd.edu/data/atmospheric_co2/mlo, accessed on 1 September 2021) and converted to partial pressure units for input to the P model.

2.4. C_3 versus C_4 Photosynthesis

The FvCB model relates to the predominant C_3 photosynthetic pathway. C_4 plants, including important crop species present in our dataset, employ a CO_2-concentrating mechanism that calls for different formulations. The approach adopted here for modelling C_4 photosynthesis follows Cai and Prentice [16] by removing the CO_2 limitation term and applying a modified (lower) intrinsic quantum yield. Individual sites were classified as C_3 or C_4 dominated based on the predominant vegetation type as described in the available ICOS metadata. This included cases, for a number of sites, where crops with different photosynthetic pathways were grown in 2018 versus 2019 (Table A1).

3. Results

We found a strong, overall correlation between the T_{air} and LST estimates (r = 0.81), but there was marked variation among the different vegetation classes (Figure 1). There was a general tendency for air temperature to underestimate remotely sensed LST and this was especially pronounced for non-forest sites.

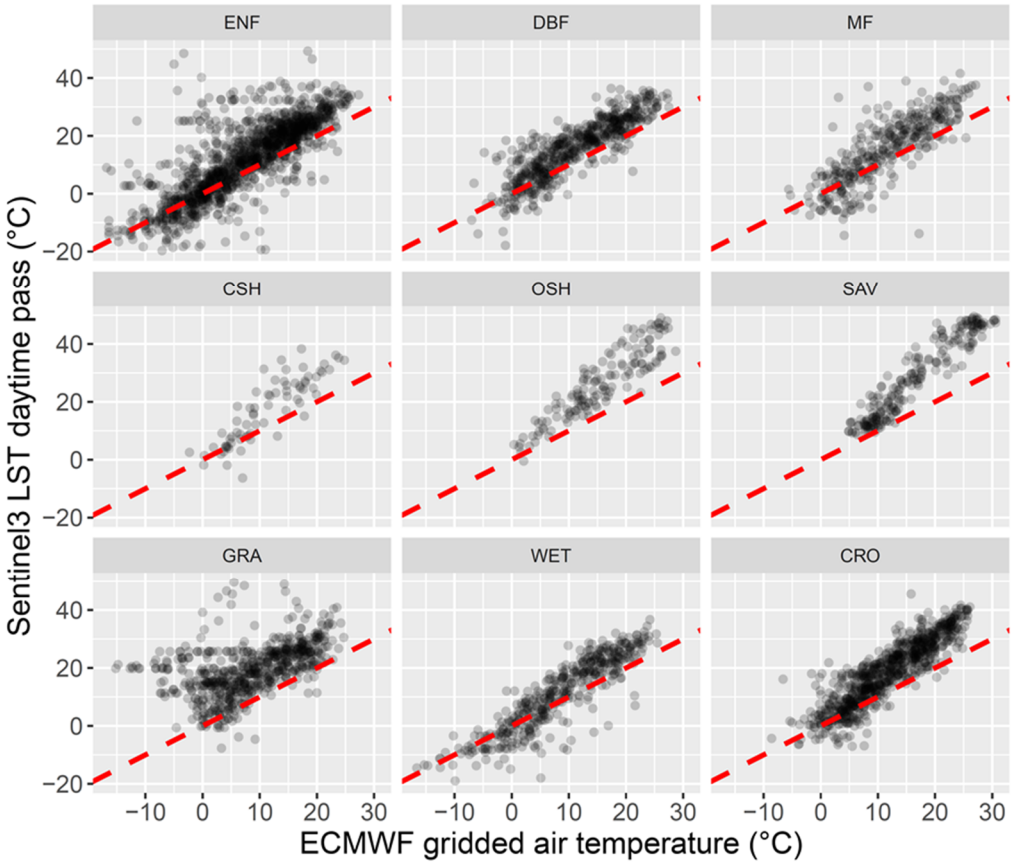

Figure 1. Scatterplots comparing ECMWF gridded air temperatures with Sentinel3 daytime LST estimates; organised by vegetation class: evergreen needleleaf forest (ENF), deciduous broadleaf forest (DBF), mixed forest (MF), closed shrublands (CSH), open shrublands (OSH), savannahs (SAV), grasslands (GRA), permanent wetlands (WET) and croplands (CRO). The dashed red line shows the ideal fit. Each point is a ten-day average.

Overall, the P-model simulations of GPP showed good agreement with the eddy-covariance values (Figure 2). There was, however, a general finding (indicated by the bias and slope metrics in Figure 2) that the simulations tended to underestimate the GPP data. Simulations forced with remotely sensed LST did not consistently perform better than the T_{air} predictions.

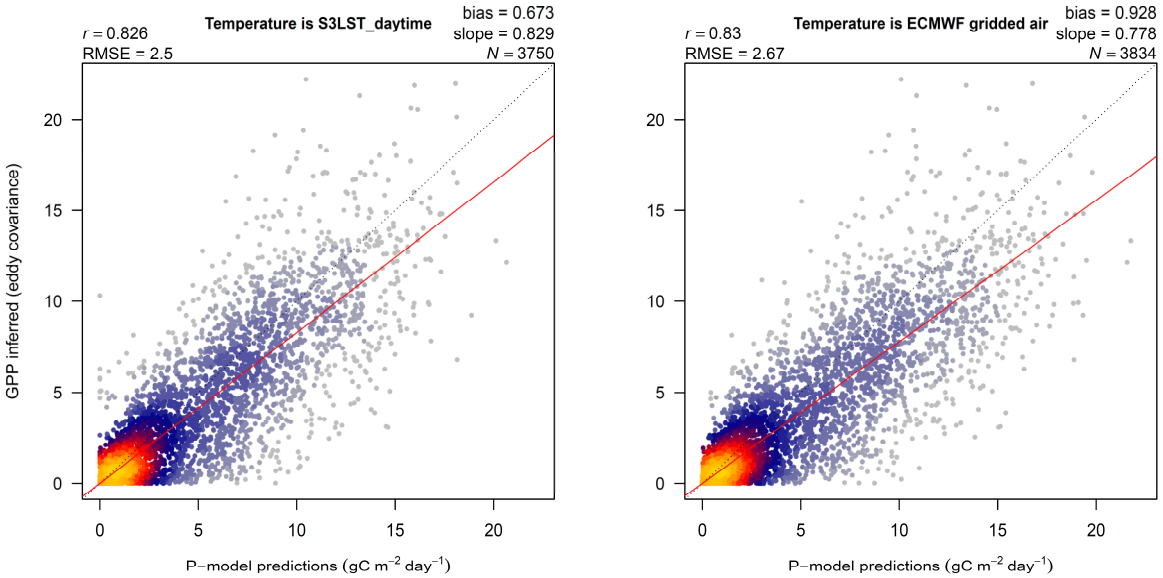

Figure 2. Goodness of fit: GPP simulations versus eddy-covariance estimates. Left panel—forcing temperature is Sentinel3 LST; Right panel—forcing temperature is ECMWF gridded air temperature. The intensity of the colours (heat-map) is designed to indicate the density of points. Each point is a ten-day average. The dashed-grey line shows the ideal fit.

A more nuanced pattern emerged, however, when relative performance was compared across vegetation categories (Figure 3). For ENF sites, the largest category in the dataset (Table A1), the two simulations were virtually indistinguishable even under drought conditions. However, for certain classes (e.g., DBF) the LST simulations performed better than T_{air}; and that advantage was enhanced in dry periods. Model performance was somewhat weaker (higher RMSE) during periods of drought.

Figure 3. Error estimation (GPP simulations versus eddy-covariance) by vegetation class with the number of participating sites indicated. Those periods identified as unusually dry (SPEI < −1.5) are shown in red and contrasted with the full timeseries (all, in blue). Bars relate to simulations driven by S3_LST and dots to ECMWF gridded T_{air}.

Time-series plots allowed us to investigate seasonal variation in model performance for individual sites; Figure 4 provides examples for contrasting vegetation classes including: Norunda in Sweden, a region where the effects of the 2018 drought were especially marked [27]; and Hesse in France, the primary site analysed in the Vicca et al. [31] study of the 2003 European drought. The P-model simulations reproduced the eddy-covariance patterns realistically, but at certain sites (e.g., Hesse in France, Figure 4) the predictions over-estimated productivity in spring. The pronounced drought of the summer of 2018 was not evident at all sites (e.g., Font-Blanche in southern France, Figure 4) and there was little evidence that productivity was markedly lower in 2018 compared to 2019. In aggregate, our analysis suggests that simulations forced with LST performed better than T_{air} equivalents for certain sites and vegetation categories—especially sparsely vegetated categories (e.g., shrublands and savannas, Figure 3). However, the predictions, even forced with LST, do not fully capture the observed effects of drought on productivity—notice the gap between eddy covariance estimates and simulations at Font-Blanche during summer 2019 (Figure 4).

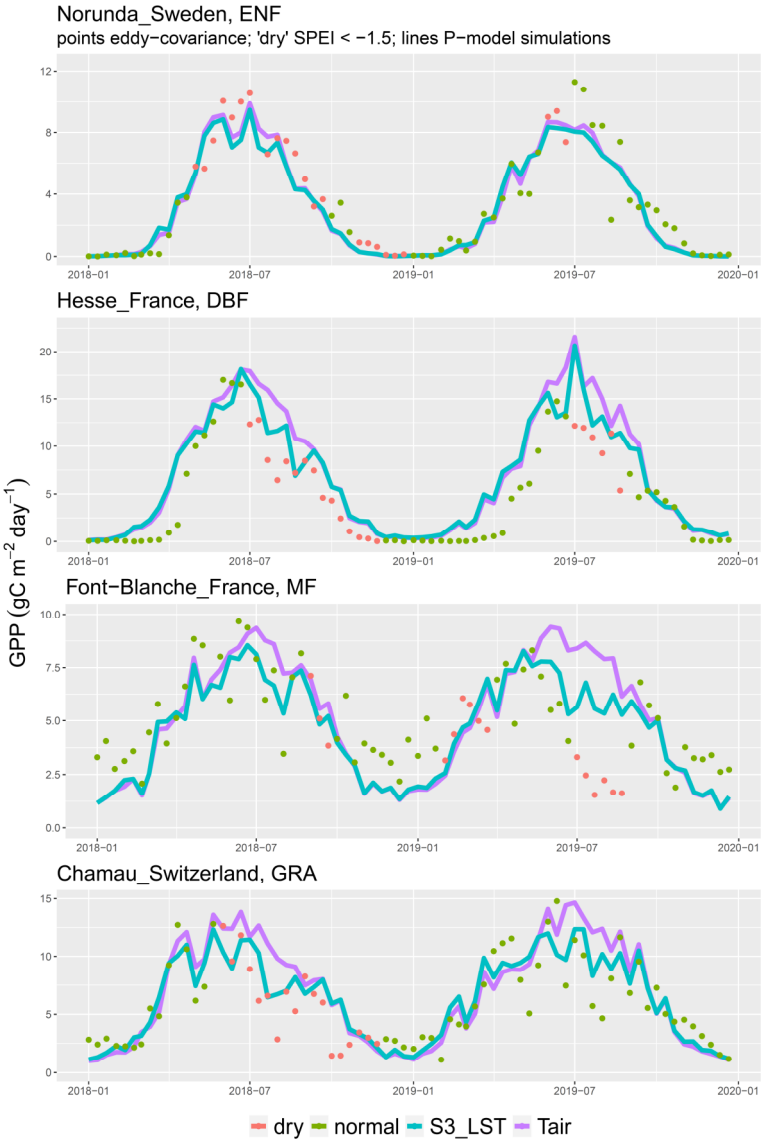

Figure 4. Seasonal variation in GPP estimates for selected sites. Inferred (eddy-covariance) values are shown as points: those periods with a site-specific SPEI < −1.5 are indicated in red. GPP simulations are shown as lines: forced with ECMWF gridded air temperature (purple) and forced with Sentinel3 daytime LST (cyan). Notice that the ranges on the y-axes vary between the plots.

4. Discussion

We found partial (site- and vegetation-dependent) support for our hypothesis that remotely sensed LST would allow better simulations of GPP than adopting equivalent measures of T_{air}. For certain categories, notably ENF, there was little to choose—even in high latitude sites where indicators of the 2018 drought were most pronounced [27]. The model performance presented here (Figure 2) compares favourably with GPP predictions reported in recent remote sensing evaluations. Using a validation dataset that partially overlaps with our own, Pablo-Moreno et al. [42] used Sentinel-2 data to predict daily GPP and achieved best results (r^2 = 0.71) with an iterative machine learning technique that selected a model with 11 variables made up of spectral bands, red-edge and near-infrared vegetation indices. In a study of seven US sites, each representing a separate biome, Zhang et al. [43] exploited the greater temporal resolution and smoother spatial distribution offered by the Ocean and Land Colour Instrument aboard Sentinel-3 to generate GPP simulations for comparison with flux tower estimates: r^2 coefficients ranged from 0.76 for a deciduous broadleaf forest to 0.45 for a grassland.

4.1. LST versus T_{air}

Even though there was evidence within our dataset that ten-day averages of daytime LST > T_{air} for most sites and PFTs, the implications for the GPP simulations were muted. This is perhaps not surprising because temperature is not the sole, or even principal, driver of variation in LUE. VPD influences LUE because of the universal response of stomata [44]—which progressively close to restrict transpiration, and hence photosynthesis, as VPD increases. As a consequence, VPD imposes important limitations on GPP [45]. Inductive multivariate modelling (avoiding a priori assumptions) applied to a daytime dataset for a forest in Germany [46] found the most important non-radiative drivers of variation in NEE to be VPD, T_{air} and wind direction—soil water content ranked in the lowest category for explanatory power. That same ranking of effects (VPD > Temperature > Soil moisture) has found support in recent modelling experiments [47].

Just as light conditions at the crown are not representative of conditions lower down the canopy, so with temperature. Temperature deltas are influenced by height [48]. If we are right to assume that remotely sensed LST can mimic the temperature of the leaf canopy, then we might expect the advantages of adopting LST rather than T_{air} to be most pronounced where the leaf area index is low (but not less than 1, see below). Our findings lend support to that expectation.

Daytime overpasses, typically mid-morning for these European sites, may not accurately reflect average conditions over the course of the daylight hours. On the other hand, many studies have reported a midday depression of photosynthetic activity [45] and so an overpass in mid-morning may often coincide with optimal conditions for photosynthesis. Might model performance be improved if we adopted a daytime average of LST rather than a single snapshot (as here)? Currently, Sentinel3 provides two overpasses in the diurnal cycle: day and night. An averaging methodology is required that will account for daylight hours as influenced by season and latitude. Early attempts (not presented here) proved unsatisfactory and must be developed further. Utilising a suite of different sensors including the Advanced Very High-Resolution Radiometer (offering increased temporal resolution and shorter revisit intervals) could help to resolve the diurnal cycle.

4.2. Possible Data Imprecisions

How can we explain the finding, at certain sites, of early season bias (GPP simulations > eddy-covariance values)? Time lags may occur between changes in greenness detected by spectral vegetation indices and photosynthetic activity [49]. For temperate deciduous species this decoupling might arise early or late in the growing season. An observed lag in GPP behind LAI during leaf emergence can be attributed to sustained investment in photosynthetic capacity beyond foliation [50]. It is also possible that these deltas arose, in part at least, from fAPAR values inflated by neighbouring vegetation not incorporated

in the flux-tower's footprint. In a study of 21 FLUXNET sites, Balzarolo et al. [51] found that the strength of the correlation between in situ and remotely sensed values of a prevalent vegetation index decreased with decreasing spatial resolution (i.e., correlations were stronger for single than for multi-pixel aggregations). The footprint of the tower (on a given day) may not correspond accurately to the pixel(s) used to generate the remotely sensed forcing variables (here, greenness and temperature) [6]. A review of high-resolution images (GoogleEarth), 1 km^2 centred on the flux-tower, suggested that around 20 of our sites might be classified as 'heterogeneous' (e.g., the sites are in close proximity to agriculture or human habitation, Table A1). A model validation exercise limited to that subset of sites classified as 'homogeneous' did not, however, provide marked improvement over the full dataset (r = 0.84 homogeneous sites, Figure A2; r = 0.83 all sites, Figure 2).

4.3. The 2018 Drought

Our measure of drought, SPEI, by focusing on climatic water balance largely ignores soil conditions. Our P-model simulations, likewise, have no explicit soil moisture term. How important might that omission be for our results? For a Mediterranean evergreen broadleaf forest, Liu et al. [52] found consistent anomalies when comparing eddy covariance GPP estimates with simulations generated by a remote sensing product (MODIS17A); those discrepancies were most pronounced during summer months of the ten-year study. The authors found that relative water content, a measure of soil water limitation, could explain ca. 75% of the GPP anomalies. Soil moisture and VPD effects can, however, be challenging to separate because low soil moisture is often accompanied by high VPD [53]. After controlling for covariation in greenness, VPD and other factors Stocker et al. (2019) concluded that soil moisture deficits were a globally important constraint on GPP inducing a global reduction of ca. 15% and amplifying the effects of extreme weather events. By contrast, Fu et al. [30], also studying the European drought of 2018, found that when soils are wet, moderate drying could have a positive effect on GPP; and that the relative importance, for GPP, of VPD and soil moisture depends on the prevailing soil water conditions, with soil moisture dominating in the driest soils.

It therefore seems likely that even if canopy temperatures are based on LST (or alternatively, for climate modelling applications, calculated using the canopy energy balance), it will be necessary to formulate responses of stomatal behaviour and photosynthetic capacity to low levels of soil moisture.

4.4. Next Steps for the Application of LST

Sparsely vegetated pixels present particular challenges for remote-sensing approaches to estimating leaf temperature because the LST values may represent a combination of bare ground as well as foliage. Sims et al. [54] evaluated a GPP model driven only by the MODIS Enhanced Vegetation Index and LST at 11 flux sites in North America and found strong correlations between eddy-covariance and modelled 16-day estimates of GPP for selected forest sites, but not for a drought-prone, shrubland site. Work is underway, supported by the spatial detail offered by high resolution satellites [55], to assess whether the Sentinel-3 LST pixel values can be usefully disaggregated to distinguish vegetation and bare ground components.

5. Conclusions

For this European dataset, incorporating a major drought event, we found good agreement between estimates of GPP inferred from eddy-covariance measurements and simulations generated using the P-model. We found that model error was higher under drought conditions as characterised by a standardised climatic index. For sparsely vegetated sites, simulations forced with land surface temperature did perform better than those forced with air temperature during periods of drought. However, our simulations, even driven by available LST estimates, do not yet reproduce the observed effects of drought on productivity.

The P-model is under continual development. There are proposals for improved formulations of the effects of temperature and soil moisture, and consideration of the role of the diffuse radiation fraction. However, the guiding principle remains seeking simplicity and generality, rather than adding complexity. Assessed against global GPP data and evaluated in terms of functional relationships of GPP to key environmental drivers, the model already performs well in comparison to considerably more complex models [47], thus offering the initial basis for a well-founded, parameter-sparse global monitoring system for GPP.

Author Contributions: Conceptualization, I.C.P., R.v.H., M.B., I.A.J., S.V. and D.G.; methodology, R.v.H., M.B., D.G., K.J.B. and I.C.P.; validation, M.B., K.J.B. and I.C.P.; writing—original draft preparation, K.J.B.; writing—review and editing, all authors. All authors have read and agreed to the published version of the manuscript.

Funding: This work received funding from the European Space Agency under the project "Development and validation of a global GPP/NPP model using MERIS and Sentinel-3 data (TerrA-P)", (ESA Contract No. 4000118570/16/I-NB, S3-4SCI LAND).

Data Availability Statement: All data used in the analysis are publicly available—relevant links are detailed in Section 2.

Acknowledgments: This work draws on the eddy covariance Warm Winter 2020 data collection acquired and shared by the ICOS community. The eddy covariance data processing and harmonisation were carried out by the ICOS Ecosystem Thematic Centre. The authors acknowledge the PIs of the eddy covariance sites and all technicians and researchers for providing their data and support to the ICOS Warm Winter 2020 dataset.

Conflicts of Interest: The authors declare no conflict of interest.

Appendix A

Table A1. Site details: longitude (negative values are west of the prime meridian); latitude (north as positive); site elevation (m above sea level); vegetation categories follow the IGBP land cover classification: evergreen needleleaf forest (ENF), deciduous broadleaf forest (DBF), mixed forest (MF), closed shrublands (CSH), open shrublands (OSH), savannahs (SAV), grasslands (GRA), permanent wetlands (WET) and croplands (CRO). spatial heterogeneity assessment (homogeneous versus heterogeneous).

Code	Sitename	Lat	Lon	Elevation (masl)	IGBP Code	Metabolism	Homogeneity
BE-Bra	Brasschaat	51.308	4.520	30	MF	C3	Homo
BE-Dor	Dorinne	50.312	4.968	248	GRA	C3	Hetero
BE-Lon	Lonzee	50.552	4.746	169	CRO	C3	Homo
BE-Maa	Maasmechelen	50.980	5.632	86	CSH	C3	Homo
BE-Vie	Vielsalm	50.305	5.998	495	MF	C3	Homo
CH-Aws	Alp Weissenstein	46.583	9.790	1969	GRA	C3	Hetero
CH-Cha	Chamau	47.210	8.410	391	GRA	C3	Hetero
CH-Dav	Davos	46.815	9.856	1652	ENF	C3	Hetero
CH-Fru	Früebüel	47.116	8.538	980	GRA	C3	Hetero
CH-Lae	Laegern	47.478	8.364	685	MF	C3	Homo
CH-Oe2	Oensingen crop	47.286	7.734	452	CRO	C3	Hetero
CZ-BK1	Bily Kriz forest	49.502	18.537	876	ENF	C3	Homo
CZ-Lnz	Lanzhot	48.682	16.946	181	MF	C3	Homo
CZ-RAJ	Rajec	49.444	16.697	653	ENF	C3	Homo

Table A1. *Cont.*

Code	Sitename	Lat	Lon	Elevation (masl)	IGBP Code	Metabolism	Homogeneity
CZ-Stn	Stitna	49.036	17.970	580	DBF	C3	Homo
CZ-wet	Trebon (CZECHWET)	49.025	14.770	426	WET	C3	Hetero
DE-Akm	Anklam	53.866	13.683	-	WET	C3	Hetero
DE-Geb	Gebesee	51.100	10.915	161	CRO	C3	Homo
DE-Gri	Grillenburg	50.950	13.513	377	GRA	C3	Hetero
DE-Hai	Hainich	51.079	10.453	467	DBF	C3	Homo
DE-HoH	Hohes Holz	52.085	11.219	220	DBF	C3	Hetero
DE-Hte	Huetelmoor	54.210	12.176	2	WET	C3	Homo
DE-Hzd	Hetzdorf	50.964	13.490	385	DBF	C3	Hetero
DE-Kli	Klingenberg	50.893	13.522	481	CRO	Rotation: C3 2018, C4 2019	Homo
DE-Obe	Oberbärenburg	50.787	13.721	755	ENF	C3	Homo
DE-RuR	Rollesbroich	50.622	6.304	515	GRA	C3	Hetero
DE-RuS	Selhausen Juelich	50.866	6.447	103	CRO	C3	Homo
DE-RuW	Wustebach	50.505	6.331	624	ENF	C3	Homo
DE-Tha	Tharandt	50.963	13.565	403	ENF	C3	Homo
DK-Sor	Soroe	55.486	11.645	52	DBF	C3	Hetero
ES-Abr	Albuera	38.702	−6.786	280	SAV	C3	Homo
ES-Agu	Aguamarga	36.940	−2.033	203	OSH	C3	Hetero
ES-LM1	Majadas del Tietar North	39.943	−5.779	264	SAV	C3	Homo
ES-LM2	Majadas del Tietar South	39.935	−5.776	269	SAV	C3	Homo
FI-Hyy	Hyytiala	61.847	24.295	190	ENF	C3	Homo
FI-Let	Lettosuo	60.642	23.960	124	ENF	C3	Homo
FI-Sii	Siikaneva	61.833	24.193	166	WET	C3	Hetero
FI-Var	Varrio	67.755	29.610	395	ENF	C3	Homo
FR-Aur	Aurade	43.550	1.106	244	CRO	C3	Homo
FR-Bil	Bilos	44.494	−0.956	39	ENF	C3	Hetero
FR-EM2	Estrees-Mons A28	49.872	3.021	85	CRO	C3	Homo
FR-FBn	Font-Blanche	43.241	5.679	434	MF	C3	Homo
FR-Fon	Fontainebleau-Barbeau	48.476	2.780	112	DBF	C3	Homo
FR-Gri	Grignon	48.844	1.952	123	CRO	C4	Homo
FR-Hes	Hesse	48.674	7.065	323	DBF	C3	Homo
FR-Lam	Lamasquere	43.496	1.238	179	CRO	Rotation: C3 2018, C4 2019	Hetero
FR-LGt	La Guette	47.323	2.284	157	WET	C3	Hetero
FR-Mej	Mejusseaume	48.118	−1.796	39	GRA	C4	Homo
IT-BFt	Bosco Fontana	45.198	10.742	42	DBF	C3	Homo
IT-BCi	Borgo Cioffi	40.524	14.957	9	CRO	C4	Hetero

Table A1. *Cont.*

Code	Sitename	Lat	Lon	Elevation (masl)	IGBP Code	Metabolism	Homogeneity
IT-Lav	Lavarone	45.956	11.281	1371	ENF	C3	Homo
IT-Lsn	Lison	45.740	12.750	-	OSH	C3	Hetero
IT-MBo	Monte Bondone	46.015	11.046	1557	GRA	C3	Homo
IT-SR2	San Rossore 2	43.732	10.291	10	ENF	C3	Homo
IT-Tor	Torgnon	45.844	7.578	2158	GRA	C3	Hetero
NL-Loo	Loobos	52.167	5.744	37	ENF	C3	Homo
RU-Fy2	Fyodorovskoye, dry spruce stand	56.448	32.902	275	ENF	C3	Homo
RU-Fyo	Fyodorovskoye	56.462	32.922	278	ENF	C3	Homo
SE-Deg	Degero	64.182	19.557	266	WET	C3	Homo
SE-Htm	Hyltemossa	56.098	13.419	123	ENF	C3	Homo
SE-Lnn	Lanna	58.341	13.102	71	CRO	C3	Homo
SE-Nor	Norunda	60.086	17.480	89	ENF	C3	Homo
SE-Ros	Rosinedal-3	64.173	19.738	168	ENF	C3	Homo
SE-Svb	Svartberget	64.256	19.775	277	ENF	C3	Homo

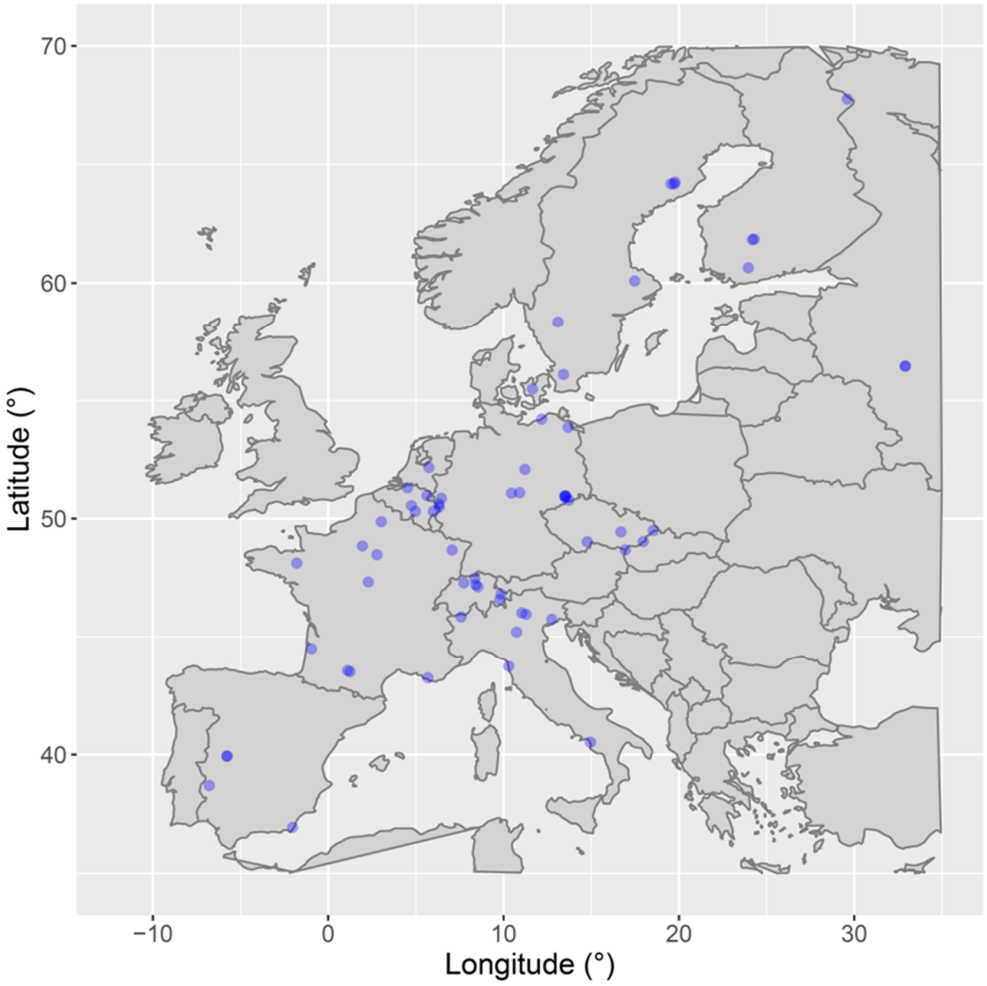

Figure A1. Map of participating sites—locations are indicated (blue dots).

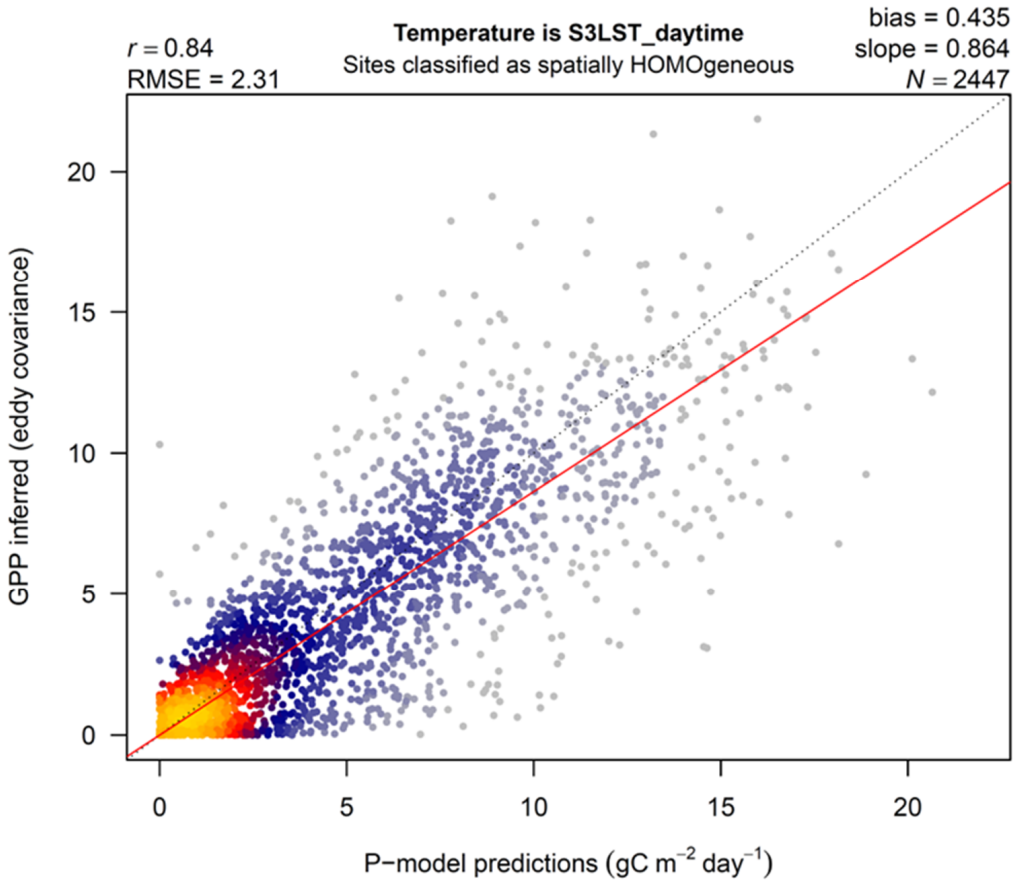

Figure A2. Model validation, GPP simulations versus eddy-covariance estimates; companion to Figure 2 (main text), but restricted to those sites deemed to show spatial homogeneity of vegetation cover. Forcing temperature is Sentinel3 LST. The intensity of the colours (heat-map) is designed to indicate the density of points. Each point is a ten-day average. The dashed-grey line shows the ideal fit.

References

1. Beer, C.; Reichstein, M.; Tomelleri, E.; Ciais, P.; Jung, M.; Carvalhais, N.; Rödenbeck, C.; Arain, M.A.; Baldocchi, D.; Bonan, G.B.; et al. Terrestrial gross carbon dioxide uptake: Global distribution and covariation with climate. *Science* **2010**, *329*, 834–838. [CrossRef] [PubMed]
2. Friedlingstein, P.; Meinshausen, M.; Arora, V.K.; Jones, C.D.; Anav, A.; Liddicoat, S.K.; Knutti, R. Uncertainties in CMIP5 Climate Projections due to Carbon Cycle Feedbacks. *J. Clim.* **2014**, *27*, 511–526. [CrossRef]
3. Baldocchi, D.D. How eddy covariance flux measurements have contributed to our understanding of Global Change Biology. *Glob. Chang. Biol.* **2020**, *26*, 242–260. [CrossRef] [PubMed]
4. Pastorello, G.; Trotta, C.; Canfora, E.; Chu, H.; Christianson, D.; Cheah, Y.-W.; Poindexter, C.; Chen, J.; Elbashandy, A.; Humphrey, M.; et al. The FLUXNET2015 dataset and the ONEFlux processing pipeline for eddy covariance data. *Sci. Data* **2020**, *7*, 225. [CrossRef]
5. Baldocchi, D.D. Assessing the eddy covariance technique for evaluating carbon dioxide exchange rates of ecosystems: Past, present and future. *Glob. Chang. Biol.* **2003**, *9*, 479–492. [CrossRef]
6. Chu, H.; Luo, X.; Ouyang, Z.; Chan, W.S.; Dengel, S.; Biraud, S.C.; Torn, M.S.; Metzger, S.; Kumar, J.; Arain, M.A.; et al. Representativeness of Eddy-Covariance flux footprints for areas surrounding AmeriFlux sites. *Agric. For. Meteorol.* **2021**, *301*, 108350. [CrossRef]
7. Farquhar, G.D.; Von Caemmerer, S.; Berry, J.A. A biochemical model of photosynthetic CO_2 assimilation in leaves of C3 species. *Planta* **1980**, *149*, 78–90. [CrossRef]
8. Medlyn, B. Physiological basis of the light use efficiency model. *Tree Physiol.* **1998**, *18*, 167–176. [CrossRef]
9. Dewar, R.C.; Medlyn, B.; McMurtrie, R.E. A mechanistic analysis of light and carbon use efficiencies. *Plant Cell Environ.* **1998**, *21*, 573–588. [CrossRef]
10. Monteith, J.L. Solar Radiation and Productivity in Tropical Ecosystems. *J. Appl. Ecol.* **1972**, *9*, 747–766. [CrossRef]
11. Monteith, J.L. Climate and the efficiency of crop production in Britain. *Philos. Trans. R. Soc. B* **1977**, *281*, 277–294. [CrossRef]
12. Zhang, J.; Wang, X.; Ren, J. Simulation of Gross Primary Productivity Using Multiple Light Use Efficiency Models. *Land* **2021**, *10*, 329. [CrossRef]

13. Prentice, I.C.; Liang, X.; Medlyn, B.E.; Wang, Y.-P. Reliable, robust and realistic: The three R's of next-generation land-surface modelling. *Atmospheric Meas. Tech.* **2015**, *15*, 5987–6005. [CrossRef]
14. Wang, H.; Prentice, I.C.; Keenan, T.F.; Davis, T.W.; Wright, I.J.; Cornwell, W.K.; Evans, B.J.; Peng, C. Towards a universal model for carbon dioxide uptake by plants. *Nat. Plants* **2017**, *3*, 734–741. [CrossRef]
15. Stocker, B.D.; Wang, H.; Smith, N.G.; Harrison, S.P.; Keenan, T.F.; Sandoval, D.; Davis, T.; Prentice, I.C. P-model v1.0: An optimality-based light use efficiency model for simulating ecosystem gross primary production. *Geosci. Model Dev.* **2020**, *13*, 1545–1581. [CrossRef]
16. Cai, W.; Prentice, I.C. Recent trends in gross primary production and their drivers: Analysis and modelling at flux-site and global scales. *Environ. Res. Lett.* **2020**, *15*, 124050. [CrossRef]
17. Bernacchi, C.J.; Pimentel, C.; Long, S.P. In vivo temperature response functions of parameters required to model RuBP-limited photosynthesis. *Plant Cell Environ.* **2003**, *26*, 1419–1430. [CrossRef]
18. Rogers, A.; Medlyn, B.E.; Dukes, J.S.; Bonan, G.; von Caemmerer, S.; Dietze, M.C.; Kattge, J.; Leakey, A.D.B.; Mercado, L.M.; Niinemets, Ü.; et al. A roadmap for improving the representation of photosynthesis in Earth system models. *New Phytol.* **2017**, *213*, 22–42. [CrossRef]
19. Bernacchi, C.J.; Singsaas, E.L.; Pimentel, C.; Portis, A.R., Jr.; Long, S.P. Improved temperature response functions for models of Rubisco-limited photosynthesis. *Plant Cell Environ.* **2001**, *24*, 253–259. [CrossRef]
20. Berry, J.A.; Bjorkman, O. Photosynthetic Response and Adaptation to Temperature in Higher Plants. *Annu. Rev. Plant Physiol.* **1980**, *31*, 491–543. [CrossRef]
21. Kumarathunge, D.P.; Medlyn, B.E.; Drake, J.; Tjoelker, M.G.; Aspinwall, M.J.; Battaglia, M.; Cano, F.J.; Carter, K.R.; Cavaleri, M.A.; Cernusak, L.A.; et al. Acclimation and adaptation components of the temperature dependence of plant photosynthesis at the global scale. *New Phytol.* **2019**, *222*, 768–784. [CrossRef] [PubMed]
22. Still, C.J.; Rastogi, B.; Page, G.F.M.; Griffith, D.M.; Sibley, A.; Schulze, M.; Hawkins, L.; Pau, S.; Detto, M.; Helliker, B.R. Imaging canopy temperature: Shedding (thermal) light on ecosystem processes. *New Phytol.* **2021**, *230*, 1746–1753. [CrossRef] [PubMed]
23. Dong, N.; Prentice, I.C.; Harrison, S.P.; Song, Q.H.; Zhang, Y.P.; Sykes, M. Biophysical homoeostasis of leaf temperature: A neglected process for vegetation and land-surface modelling. *Glob. Ecol. Biogeogr.* **2017**, *26*, 998–1007. [CrossRef]
24. Fauset, S.; Freitas, H.C.; Galbraith, D.R.; Sullivan, M.J.; Aidar, M.P.; Joly, C.A.; Phillips, O.L.; Vieira, S.A.; Gloor, M.U. Differences in leaf thermoregulation and water use strategies between three co-occurring Atlantic forest tree species. *Plant Cell Environ.* **2018**, *41*, 1618–1631. [CrossRef]
25. Cowan, I.; Farquhar, G. Stomatal function in relation to leaf metabolism and environment. In *Integration of Activity in Higher Plants*; Jennings, D., Ed.; Cambridge University Press: Cambridge, UK, 1977; pp. 471–505.
26. Medlyn, B.E.; Duursma, R.A.; Eamus, D.; Ellsworth, D.S.; Prentice, I.C.; Barton, C.V.M.; Crous, K.Y.; De Angelis, P.; Freeman, M.; Wingate, L. Reconciling the optimal and empirical approaches to modelling stomatal conductance. *Glob. Chang. Biol.* **2011**, *17*, 2134–2144. [CrossRef]
27. Buras, A.; Rammig, A.; Zang, C.S. Quantifying impacts of the 2018 drought on European ecosystems in comparison to 2003. *Biogeosciences* **2020**, *17*, 1655–1672. [CrossRef]
28. Ciais, P.; Reichstein, M.; Viovy, N.; Granier, A.; Ogée, J.; Allard, V.; Aubinet, M.; Buchmann, N.; Bernhofer, C.; Carrara, A.; et al. Europe-wide reduction in primary productivity caused by the heat and drought in 2003. *Nature* **2005**, *437*, 529–533. [CrossRef]
29. Vereecken, H.; Schnepf, A.; Hopmans, J.; Javaux, M.; Or, D.; Roose, T.; Vanderborght, J.; Young, M.; Amelung, W.; Aitkenhead, M.; et al. Modeling Soil Processes: Review, Key Challenges, and New Perspectives. *Vadose Zone J.* **2016**, *15*, 1–57. [CrossRef]
30. Fu, Z.; Ciais, P.; Prentice, I.C.; Gentine, P.; Makowski, D.; Bastos, A.; Luo, X.; Green, J.K.; Stoy, P.C.; Yang, H.; et al. Atmospheric dryness reduces photosynthesis along a large range of soil water deficits. *Nat. Commun.* **2022**, *13*, 989. [CrossRef]
31. Vicca, S.; Balzarolo, M.; Filella, I.; Granier, A.; Herbst, M.; Knohl, A.; Longdoz, B.; Mund, M.; Nagy, Z.; Pintér, K.; et al. Remotely-sensed detection of effects of extreme droughts on gross primary production. *Sci. Rep.* **2016**, *6*, 28269. [CrossRef]
32. Stocker, B.D.; Zscheischler, J.; Keenan, T.F.; Prentice, I.C.; Peñuelas, J.; Seneviratne, S.I. Quantifying soil moisture impacts on light use efficiency across biomes. *New Phytol.* **2018**, *218*, 1430–1449. [CrossRef]
33. Zhou, S.; Duursma, R.A.; Medlyn, B.E.; Kelly, J.W.; Prentice, I.C. How should we model plant responses to drought? An analysis of stomatal and non-stomatal responses to water stress. *Agric. For. Meteorol.* **2013**, *182*, 204–214. [CrossRef]
34. Stocker, B.D.; Zscheischler, J.; Keenan, T.F.; Prentice, I.C.; Seneviratne, S.I.; Peñuelas, J. Drought impacts on terrestrial primary production underestimated by satellite monitoring. *Nat. Geosci.* **2019**, *12*, 264–270. [CrossRef]
35. Slette, I.J.; Post, A.K.; Awad, M.; Even, T.; Punzalan, A.; Williams, S.; Smith, M.D.; Knapp, A.K. How ecologists define drought, and why we should do better. *Glob. Chang. Biol.* **2019**, *25*, 3193–3200. [CrossRef]
36. Vicente-Serrano, S.M.; Beguería, S.; López-Moreno, J.I. A Multiscalar Drought Index Sensitive to Global Warming: The Standardized Precipitation Evapotranspiration Index. *J. Clim.* **2010**, *23*, 1696–1718. [CrossRef]
37. R Core Team. *R: A Language and Environment for Statistical Computing*; R Foundation for Statistical Computing: Vienna, Austria, 2020; Available online: http://www.R-project.org (accessed on 15 February 2023).
38. Stocker, B.D. rpmodel v1.0.4. Available online: https://zenodo.org/record/3560169#.ZBl05HZBxD8 (accessed on 15 February 2023).
39. Meek, D.W.; Hatfield, J.L.; Howell, T.A.; Idso, S.B.; Reginato, R.J. A Generalized Relationship between Photosynthetically Active Radiation and Solar Radiation. *Agron. J.* **1984**, *76*, 939–945. [CrossRef]

40. Allen, R.; Pereira, L.; Raes, D.; Smith, M. *Crop Evapotranspiration-Guidelines for Computing Crop Water Requirements*; FAO: Rome, Italy, 1998; p. 56. Available online: http://www.fao.org/docrep/x0490e/x0490e00.htm (accessed on 26 October 2022).
41. Ghent, D.; Dodd, E.; Veal, K.; Perry, M.; Jimenez, C.; Ermida, S. CCI Land Surface Temperature Algorithm Theoretical Basis Document. LST-CCI-D2.2-ATBD. 2021. Available online: https://admin.climate.esa.int/media/documents/LST-CCI-D2.2-ATBD_-_i3r0_-_Algorithm_Theoretical_Basis_Document.pdf (accessed on 15 February 2023).
42. Pabon-Moreno, D.E.; Migliavacca, M.; Reichstein, M.; Mahecha, M.D. On the Potential of Sentinel-2 for Estimating Gross Primary Production. *IEEE Trans. Geosci. Remote Sens.* **2022**, *60*, 4409412. [CrossRef]
43. Zhang, Z.; Zhao, L.; Lin, A. Evaluating the Performance of Sentinel-3A OLCI Land Products for Gross Primary Productivity Estimation Using AmeriFlux Data. *Remote Sens.* **2020**, *12*, 1927. [CrossRef]
44. Grossiord, C.; Buckley, T.N.; Cernusak, L.A.; Novick, K.A.; Poulter, B.; Siegwolf, R.T.W.; Sperry, J.S.; McDowell, N.G. Plant responses to rising vapor pressure deficit. *New Phytol.* **2020**, *226*, 1550–1566. [CrossRef]
45. Lasslop, G.; Reichstein, M.; Papale, D.; Richardson, A.D.; Arneth, A.; Barr, A.; Stoy, P.; Wohlfahrt, G. Separation of net ecosystem exchange into assimilation and respiration using a light response curve approach: Critical issues and global evaluation. *Glob. Chang. Biol.* **2010**, *16*, 187–208. [CrossRef]
46. Moffat, A.M.; Beckstein, C.; Churkina, G.; Mund, M.; Heimann, M. Characterization of ecosystem responses to climatic controls using artificial neural networks. *Glob. Chang. Biol.* **2010**, *16*, 2737–2749. [CrossRef]
47. Bloomfield, K.J.; Stocker, B.D.; Keenan, T.F.; Prentice, I.C. Environmental controls on the light use efficiency of terrestrial gross primary production. *Glob. Chang. Biol.* **2023**, *29*, 1037–1053. [CrossRef] [PubMed]
48. Miller, B.D.; Carter, K.R.; Reed, S.C.; Wood, T.E.; Cavaleri, M.A. Only sun-lit leaves of the uppermost canopy exceed both air temperature and photosynthetic thermal optima in a wet tropical forest. *Agric. For. Meteorol.* **2021**, *301*, 108347. [CrossRef]
49. Maleki, M.; Arriga, N.; Barrios, J.M.; Wieneke, S.; Liu, Q.; Peñuelas, J.; Janssens, I.A.; Balzarolo, M. Estimation of Gross Primary Productivity (GPP) Phenology of a Short-Rotation Plantation Using Remotely Sensed Indices Derived from Sentinel-2 Images. *Remote Sens.* **2020**, *12*, 2104. [CrossRef]
50. Barr, A.G.; Black, T.A.; Hogg, E.H.; Griffis, T.J.; Morgenstern, K.; Kljun, N.; Theede, A.; Nesic, Z. Climatic controls on the carbon and water balances of a boreal aspen forest, 1994–2003. *Glob. Chang. Biol.* **2007**, *13*, 561–576. [CrossRef]
51. Balzarolo, M.; Peñuelas, J.; Veroustraete, F. Influence of Landscape Heterogeneity and Spatial Resolution in Multi-Temporal In Situ and MODIS NDVI Data Proxies for Seasonal GPP Dynamics. *Remote Sens.* **2019**, *11*, 1656. [CrossRef]
52. Liu, J.; Rambal, S.; Mouillot, F. Soil Drought Anomalies in MODIS GPP of a Mediterranean Broadleaved Evergreen Forest. *Remote Sens.* **2015**, *7*, 1154–1180. [CrossRef]
53. Novick, K.A.; Ficklin, D.L.; Stoy, P.C.; Williams, C.A.; Bohrer, G.; Oishi, A.C.; Papuga, S.A.; Blanken, P.D.; Noormets, A.; Sulman, B.N.; et al. The increasing importance of atmospheric demand for ecosystem water and carbon fluxes. *Nat. Clim. Chang.* **2016**, *6*, 1023–1027. [CrossRef]
54. Sims, D.A.; Rahman, A.F.; Cordova, V.D.; El-Masri, B.Z.; Baldocchi, D.D.; Bolstad, P.V.; Flanagan, L.B.; Goldstein, A.H.; Hollinger, D.Y.; Misson, L.; et al. A new model of gross primary productivity for North American ecosystems based solely on the enhanced vegetation index and land surface temperature from MODIS. *Remote Sens. Environ.* **2008**, *112*, 1633–1646. [CrossRef]
55. Guzinski, R.; Nieto, H.; Sandholt, I.; Karamitilios, G. Modelling High-Resolution Actual Evapotranspiration through Sentinel-2 and Sentinel-3 Data Fusion. *Remote Sens.* **2020**, *12*, 1433. [CrossRef]